J Therm Spray Tech (2026) 35:577–590
https://doi.org/10.1007/s11666-025-02093-2

ORIGINAL RESEARCH ARTICLE

Investigation of the Process Stability and Effectiveness Using a Multi-Arc Spraying Torch with Axial Suspension Injection

J. Schmitt[1] · S. Zimmermann[2] · C. Kirner[2] · R. Vaßen[1,3] · J. Schein[2] · G. Mauer[1,4]

Submitted: 4 July 2025 / in revised form: 26 August 2025 / Accepted: 22 September 2025 / Published online: 28 October 2025

Abstract The Axial III^{TM} torch is a multi-arc plasma generator equipped with three single cathode–anode units. It is widely used for suspension plasma spraying because of its axial feedstock injection. Previous work has shown that the plasma jet is not completely homogeneous, due to power fluctuations and the triple distribution of the plasma enthalpy. This could affect the stability and efficiency of the spraying process. Therefore, state-of-the-art process diagnostics were used to further characterize the process. The plasma characteristics were studied at three different compositions while spraying a 30% wt.% Y_2O_2 water-based suspension using two different nozzle geometries. Time-resolved measurements of voltages and currents were used to gain insight into the arc dynamics and the plasma-suspension interaction. The resulting in-flight particle temperatures and velocities were analyzed using the Accuraspray 4.0. The specific plasma gas composition, particularly the nitrogen content, affected the temperature and transport coefficients of the plasma and thus the particle characteristics. These factors, in turn, directly affected the deposition efficiency and the microstructure of the resulting coatings, as demonstrated by the experiments. Meanwhile, the overall process efficiency decreased for the nozzle with the reduced expansion ratio. This study provides the basis for deriving measures to improve the stability and efficiency of suspension plasma spraying.

Keywords particle diagnostic · process effectiveness · process stability · suspension plasma spray · thermal spray

This article is an invited paper selected from presentations at the 2025 International Thermal Spray Conference, held May 5–8, 2025, in Vancouver, Canada, and has been expanded from the original presentation. The issue was organized by Giovanni Bolelli, University of Modena and Reggio Emilia (Lead Editor); Fardad Azarmi, North Dakota State University; Sara Bagherifard, Politecnico di Milano; Partha Pratim Bandyopadhyay, Indian Institute of Technology, Kharagpur; Šárka Houdková, University of West Bohemia; Heli Koivuluoto, Tampere University; Yuk-Chiu Lau, General Electric Power (Retired); Hua Li, Ningbo Institute of Materials Technology and Engineering, CAS; Sinan Müftü, Northeastern University; and Filofteia-Laura Toma, Fraunhofer Institute for Material and Beam Technology.

✉ J. Schmitt
jo.schmitt@fz-juelich.de

[1] Institute of Energy Materials and Devices (IMD-2), Forschungszentrum Jülich GmbH, Jülich, Germany

[2] Institute of Physics, University of the Bundeswehr Munich, Neubiberg, Germany

[3] Institut für Werkstoffe, Ruhr-Universität Bochum, Bochum, Germany

[4] Department of Mechanical Engineering, Technische Universität Dortmund, Dortmund, Germany

Abbreviations

CEA	Chemical equilibrium application
DE	Deposition efficiency
DVC	Dense vertical cracks
SiO_2	Silicon dioxide
SPS	Suspension plasma spray
TBC	Thermal barrier coating

List of Symbols

d	Particle diameter (µm)
Por	Porosity (%)
R_a	Arithmetic mean surface roughness (µm)
$R_{a,Volt}$	Arithmetic mean voltage roughness (µm)
$R_{z,Volt}$	Maximum height, roughness profile (µm)
t_c	Coating thickness (mm)
T_p	Particle temperature (°C)
T_S	Surface temperature (°C)

V_m Mean voltage (V)
v_p Particle velocity (m/s)

Subscripts

I, II, III Ar-based case, N_2-Ar case, N_2-based case, respectively
n1, n2 Nozzle 1 = 5/16″, Nozzle 2 = 7/16

Introduction

The Axial III^{TM} torch, (Northwest Mettech Corp., Surrey, BC, Canada), is a multi-arc plasma generator designed for thermal spraying applications. The torch consists of three independent single cathode–anode units that allow the generation of three individual arcs that converge to form a unified plasma jet. One of the primary advantages of this configuration is the enhanced stability it provides over traditional single cathode torches. The splitting of power into multiple arcs reduces fluctuations in the plasma jet, thereby enhancing its consistency and reliability (Ref 1-4).

The operating characteristics of the Axial III^{TM} torch allow for effective axial injection of feedstock materials directly into the center of the plasma stream. This method serves to mitigate the adverse effects associated with radial injection, such as the introduction of variations in particle treatment due to turbulence in the outer plasma fringes (Ref 5). Consequently, this design facilitates extensive melting of injected powders and supports high deposition rates and efficiencies (Ref 6). Furthermore, the ability to achieve high impact velocities—up to 800 m/s—also allows for effective coating of rough surfaces without the need for a smooth substrate, thus broadening the scope of thermal spraying (Ref 7, 8). Furthermore, the Axial III^{TM} torch is a technique for managing high-enthalpy gases with a high nitrogen content. The resulting plasma has been shown to be advantageous in the melting of powder particles, thereby enhancing the deposition efficiency (DE) at a reduced overall production cost (Ref 9). Plasma spray experiments using a high nitrogen content, as carried out by Lima et al. (Ref 10), demonstrated a significant increase in DE and cost reduction. Conventional torch design yielded disadvantages regarding the heat load and thus resulting nozzle erosion for the usage of high-enthalpy plasmas (Ref 11). Therefore, the Axial III^{TM} torch design's three cathode–anode configuration is a technique to reduce the heat load per plasma generator. This, in turn, enables larger nitrogen content and thus increased process efficiency.

Recent studies have focused on the interaction between the thermal plasma jet and axially injected suspension droplets. Gaudin et al. investigated axial particle injection of Y_2O_3 suspension using optical and thermal diagnostics. A negligible influence of the atomizing gas (referred to as co-injector gas) on the microstructure was observed (Ref 12). The simulation of the Axial III^{TM} torch and its arc fluctuations has also been subject of studies by Perambadur et al. (Ref 13), where the authors created a digital twin to investigate the electric arc motion.

Lee et al. observed a significant fragmentation of the formed droplets as a result of their interaction with the plasma, which in turn affects the volume of the deposited splats. They found that this volume is very similar to that of individual solid feedstock particles, regardless of droplet size or solid content (Ref 14). Furthermore, Tarasi et al. (Ref 15, 16) investigated the in-flight characteristics of powder particles sprayed with the Axial III^{TM} torch, including their velocities and temperatures, and correlated these parameters with coating properties. Diagnostic studies of the Axial III^{TM} torch from Zimmermann et al. (Ref 17) revealed the existence of a triple temperature distribution in the plasma jet, with three distinct lobes observed around the jet axis. The total plasma power showed rapid fluctuations due to variations in the three cathode–anode units, resulting in spatial and temporal temperature inhomogeneities. Furthermore, electrode wear reduces the total plasma power and leads to enthalpy asymmetries. Increasing the axial carrier gas flow resulted in a radial constriction of the jet, which may have reduced plasma enthalpy but did not adversely affect performance. In addition, the study indicated the potential for demixing of gas constituents, a common issue in plasma jets with varying gas densities. These findings are crucial to optimizing the operating parameters Axial III^{TM} torch's (Ref 17). Such degradation or wear effects on multi-electrode plasma torches have also been subject of studies (Ref 18), in line with approaches to generally simulate the suspension plasma spray process (Ref 19).

This study takes an integrated approach, combining particle diagnostics, in situ current–voltage measurements, and coating evaluation within a single framework. While many previous studies have focused on plasma spray torches, such as the Triplex torch, the present study considers the Axial III^{Tm} torch. This system is able to process comparatively high nitrogen content. Consequently, this study involves a targeted comparison of parameters between coatings sprayed with high and low nitrogen content. Particular attention is paid to the high energy consumption of SPS, especially due to liquid evaporation. Building on our previous study (Ref 17), three different gas compositions were studied using the Axial III^{Tm} torch with two different nozzle diameters. Considering the transport coefficients of the respective plasma, emphasis is placed on in-flight particle diagnostics and coating evaluation obtained with the respective gas mixture. Furthermore, voltage and current measurements were performed for all three individual cathode–anode units.

Experimental Methods

Plasma Spray Environment

The setup for all experiments was a complete Axial III™ plasma generator with three EPP-601 electrical power sources (ESAB AB, Laxå, Sweden). Two converging-diverging nozzles with a throat diameter of 7.94 mm (5/16″, n1) and 11.25 mm (7/16″, n2), respectively, and the same outlet diameter have been used for the experiments. The expansion ratio in the divergent section of the 7/16”-nozzle decreases and is expected to affect the plasma and particle properties (Ref 20). The dimensions are given in Table 1.

A Treibacher AuerCoat Y_2O_3 30 wt.% T1 (SUS 633 T, water-based) was used as suspension. The particle diameters were d_{10} = 0.4 µm, d_{50} = 2.5 µm and d_{90} = 5 µm, respectively. The parameters of the plasma generator studied in this work are summarized in Table 2. The plasma typically consists out of Ar, N_2 and H_2 in varying proportions, where the total gas flow was the same in each case. The suspension feed rate was set at 45 ml/min in each case. The spray distance was 100 mm and the surface scanning speed of the robot was set at 1500 mm/s. Based on preliminary experiments, a 1 s break was set between each spray meander for a total number of 20 spray passes. Spraying was performed on stainless steel substrates (AISI 316Ti, 30 mm × 23 mm and 25 mm × 25 mm), that had previously been grit blasted with F36 (Al_2O_3, 425-600 µm) before. All samples were cooled by compressed air on the backside.

Characterization Methods

To evaluate the deposition efficiency (DE), which is the ratio of the total material sprayed to the material that was actually deposited, each sample was weighed before and after the deposition. The thickness of the substrate and the as-sprayed specimens were evaluated by using a micrometer caliper.

Topography was analyzed using an optical profilometer with a CHR10000 sensor (model CT350T, cyber-TECHNOLOGIES GmbH, Germany). The roughness measurements of all coatings were carried out with the same device and a CHR1000 sensor, which provides a higher resolution. Here, the sample surface was scanned over 5 line profiles in the horizontal and vertical directions, each 20 mm in length and spaced by 1 mm, with a step size of 1 µm.

To study the microstructure, the following procedure was used: sectioning the coated specimen in the middle with a wire saw HDS 25 (well Diamantdrahtsägen GmbH, Mannheim, Germany), grounding and polishing until the final step with SiO_2-suspension using the ATM Saphir 550 (Struers GmbH, Germany).

A Zeiss GeminiSEM450 scanning electron microscope (Zeiss, Oberkochen, Germany) was used to observe the microstructure of the polished cross sections. Porosity was obtained graphically by evaluating seven images of the same scale in the software ImageJ (Ref 21).

Plasma and Particle Diagnostics

Particle diagnostics were performed using the Accuraspray 4.0 (TECNAR Automation Ltd., St-Bruno, Qc, Canada). This device is an in-line thermal spray sensor that measures the spray plume temperature, velocity, dimension, orientation, intensity and stability. The measurement is based on an ensemble method that provides averaged values from the intensity maximum of the particle jet. The particle temperature is obtained via two color pyrometry, where the radiation intensity from the particle is evaluated at two wavelengths. The particle velocity is determined by means of the “time of flight” method, where the emitted ration from particles is measured at two defined locations along the spray direction. Particle data have been obtained over a period of 60 s at a standoff distance of 100 mm in radial direction to the plume. A more detailed explanation of the measurement principle is given elsewhere (Ref 22).

Table 2 Applied gas composition in this study

Case	Ar, slpm	N_2, slpm	H_2, slpm	Total, slpm
I	75%	15%	10%	220
Ar-based	165	33	22	
II N_2-Ar	25%	60%	15%	220
	55	132	33	
III N_2-based	0%	75%	25%	220
	0	165	55	

Current was set to I = 220 A for each generator.

slpm, standard liters per minute.

Table 1 Dimensions of the 5/16″ and 7/16 nozzles

Nozzle	Throat diameter, mm	Divergent length, mm	Exit diameter, mm	Expansion ratio
5/16″, n1	7.93	6.60	14.60	3.39
7/16″, n2	11.11	5.20	14.60	1.73

The current–voltage measurements were performed with the following experimental settings (Ref 17):

- 3 × current measurements with Chauvin Arnoux AC-DC Current Clamp PA 22 (1 mV/A), 1 × current determination (total current) with Chauvin Arnoux AC-DC Current Clamp PA 22 (1 mV/A).
- Voltage measurements with TT-SI-9001 Differential Probe (1/100) at different points (Generator_1 (red), Generator_2 (green) and Generator_3 (blue) in Fig. 3).
- Data processing with 1 × Multi_Detect_Control_MDC1_CGS (40 MS/s, 12 bit, 8 channels).
- Total recording time: 20 ms (10 buffers of 2 ms each with 80001 data points), 800010 single data points.
- Additional side-imaging of the different plasma-jets with PCO-Dimax HS4 (high-speed camera).

Results and Discussion

Analysis of the Plasma Properties

The thermophysical properties of the gas composition in Table 2 were analyzed using computational simulations performed with the Chemical Equilibrium Application (CEA2) software at a pressure set to 0.1 MPa (Ref 23). Geometrical conditions of the nozzle are considered by using the "Rocket Feature." The thermal conductivity and viscosity were calculated for a wide range of temperatures that are typical of such plasmas using the Axial III^{TM} torch under specified conditions. These parameters are of great interest for the characterization of the plasma since they affect, for example, the plasma velocity, density or heat transfer to the particles (Ref 24).

The calculation of the transport coefficients is based, among other things, on the specific nozzle geometry. Therefore, it is evident that the absolute values vary between 5/16" and 7/16" nozzles. However, it was initially assumed that the ranking between each case will remain constant, as demonstrated by the results presented later. The results for the 5/16" nozzle are therefore presented in the following section.

The thermal conductivity of the gas composition increases due to dissociation and ionization phenomena (see Fig. 1a). Dissociation becomes significant at elevated temperatures, with molecular nitrogen exhibiting significant dissociation starting at about 5000 K, while hydrogen begins to dissociate at temperatures as low as 2500 K. Ionization, which predominantly involves radicals and elemental species, is observed to begin at about 10 000 K. These processes increase the thermal conductivity due to the increased reactional portion of the thermal conductivity (Ref 24). Among the gas composition analyzed, pure argon has the lowest thermal conductivity. This behavior is attributed to the monatomic nature of argon and the absence of molecular dissociation under the conditions studied. In contrast, mixtures with higher molecular fractions, such as nitrogen or hydrogen-rich gas, show the highest thermal conductivity due to the high degree of dissociation which contributes to the heat transport.

The viscosity of the gas composition in Fig. 1(b) increases up to the temperatures where the collision of neutrals reaches its maximum and ionization begins at about 10 000 K. With increasing ionization, long-range Coulomb interactions between charged particles reduce the interactions between the gas particles and thus, the viscosity decreases again (Ref 24). The downward trend ends when ionization is complete. Unlike thermal conductivity, the scaling of viscosity with molecular fraction is less pronounced. Here, the gas mixture with the highest molecular fraction has the lowest viscosity.

If the gas has a high thermal conductivity, which is the case for larger molecular fractions of nitrogen and hydrogen, the arc will be subject to greater constriction, resulting in an increase in electrical resistance (Ref 25). As a result, a higher voltage is required to obtain the set current when the gas mixture has a higher thermal conductivity. This increases the power and therefore the plasma enthalpy.

This effect is reflected in the power balance of the plasma generators. The input power for each gas mixture, which has been obtained directly by measuring the voltages and currents at the three cathodes and anodes of the spray torch, is shown in Fig. 2. As can be seen from the thermal conductivity data, the highest input power is obtained with the highest content of nitrogen and hydrogen. The lowest thermal conductivity for the Ar-based case gives the lowest input power, while the N_2-Ar case is in between the other two. Since the torch must be cooled during operation, a portion of the input power is dissipated. Taking this cooling power into account, the efficiency of the torch can be calculated as the ratio of the net power to the input power, where the former is the difference between the input power and the cooling power. It has already been mentioned that when the thermal conductivity of the plasma gas is high, the arc is constricted. Therefore, the heat transfer from the arcs to the anode walls is less efficient. Consequently, a lower cooling capacity is required in relation to the total input power. This can be seen from the calculated efficiencies. Although the required cooling power is highest for the N_2-based case, the torch efficiency is best for this case. In contrast, the Ar-based case has the lowest efficiency at the lowest input power.

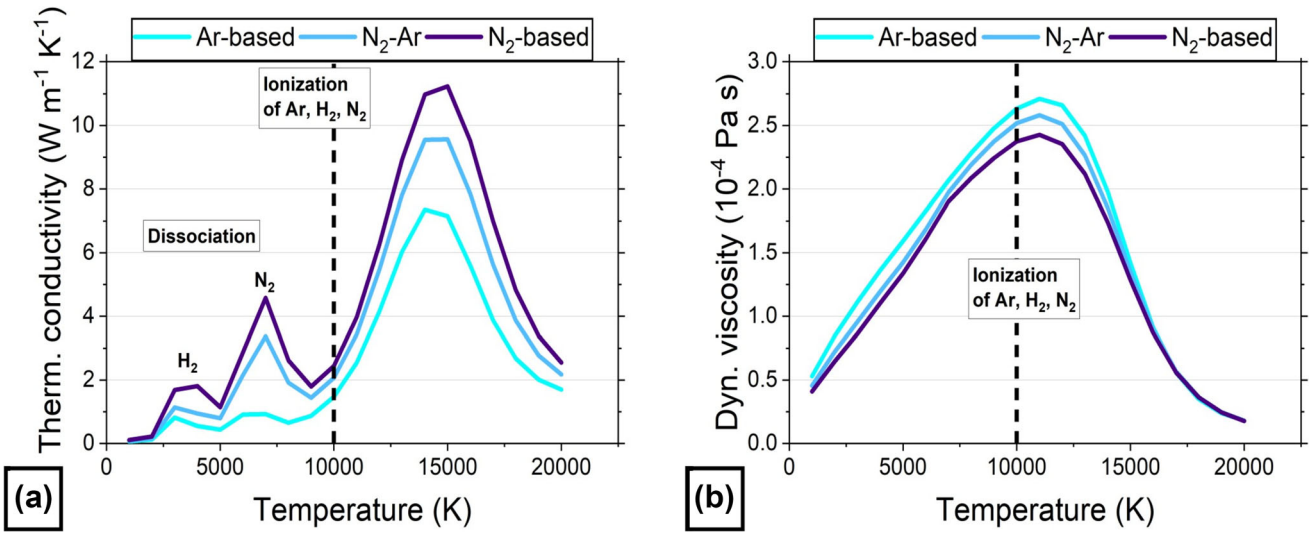

Fig. 1 Thermal conductivity (a) and Dynamic viscosity (b) for each of the three plasma condition

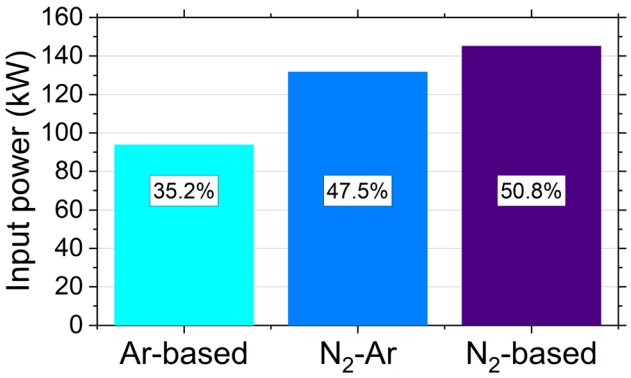

Fig. 2 Input power for the three plasma conditions; in addition, the corresponding torch efficiency is included for each condition

5/16″ Nozzle

Current and Voltage Measurements

Current and voltage data were obtained as described in the 'Experimental Methods' section. The frequency distributions of the voltage values are plotted in Fig. 3 for each of the three arc generators in the Axial III^{TM} torch. The initial current was set to 220 A for each case. Each color (red, green, blue) can be assigned to a single plasma generator (Unit 1, 2, 3). The Ar-based case (a), the N_2-Ar case (b) and the N_2-based case (c) are representative of spray experiments performed without suspension. The identical set of statistics (such as mean, standard deviation or variation) for the comparison of the three parameters was calculated by a self-written evaluation software. The class width of the respective distribution was selected to ensure that there was sufficient number of turning points, without being biased by individual data points.

As already shown by Zimmermann et al. (Ref 17), the three plasma generators produce different frequency distributions of the voltage at (almost constant) current. Furthermore, this change is also clearly visible when the gas composition is varied. The different instabilities are a characteristic voltage feature of single cathode–single anode plasma generators, such as those installed in the Axial III^{TM} torch. Based on our previous study (Ref 17), the three intensity lobes are also present within the voltage measurements. Furthermore, the respective input power is correlated to the voltage value of the frequency distribution for the individual parameters.

The results show that the mean voltage values increase with the thermal conductivity of the gas mixture. It is also visible that the frequency distributions are only symmetric for the N_2-Ar case with a slightly higher values for Unit 3. In comparison with the Gaussian-shaped distribution, the Ar-based case yields a non-symmetric distribution around the mean values with a shifted maximum. Overall, the frequency distribution look more flattened compared to the N_2-Ar case. The first two cases revealed an overall good alignment of each plasma unit for the respective gas mixture. The frequency distribution of the voltage values for the N_2-based case is symmetric but to a different extent around the mean values. While Unit 1 and 2 yield a consistent trend, Unit 3 shows a differing course. As already evident in the N_2-Ar case, the plasma generators in Unit 3 also show the biggest variations. These results are similar to the findings from the transport coefficients and the power supply, where the Ar-based case was much lower.

Additional analyses of the current have been evaluated in the same way. It was found that the current, which was set at 220 A, was also subject to fluctuations. These typically averaged around ± 5 A, and the frequency

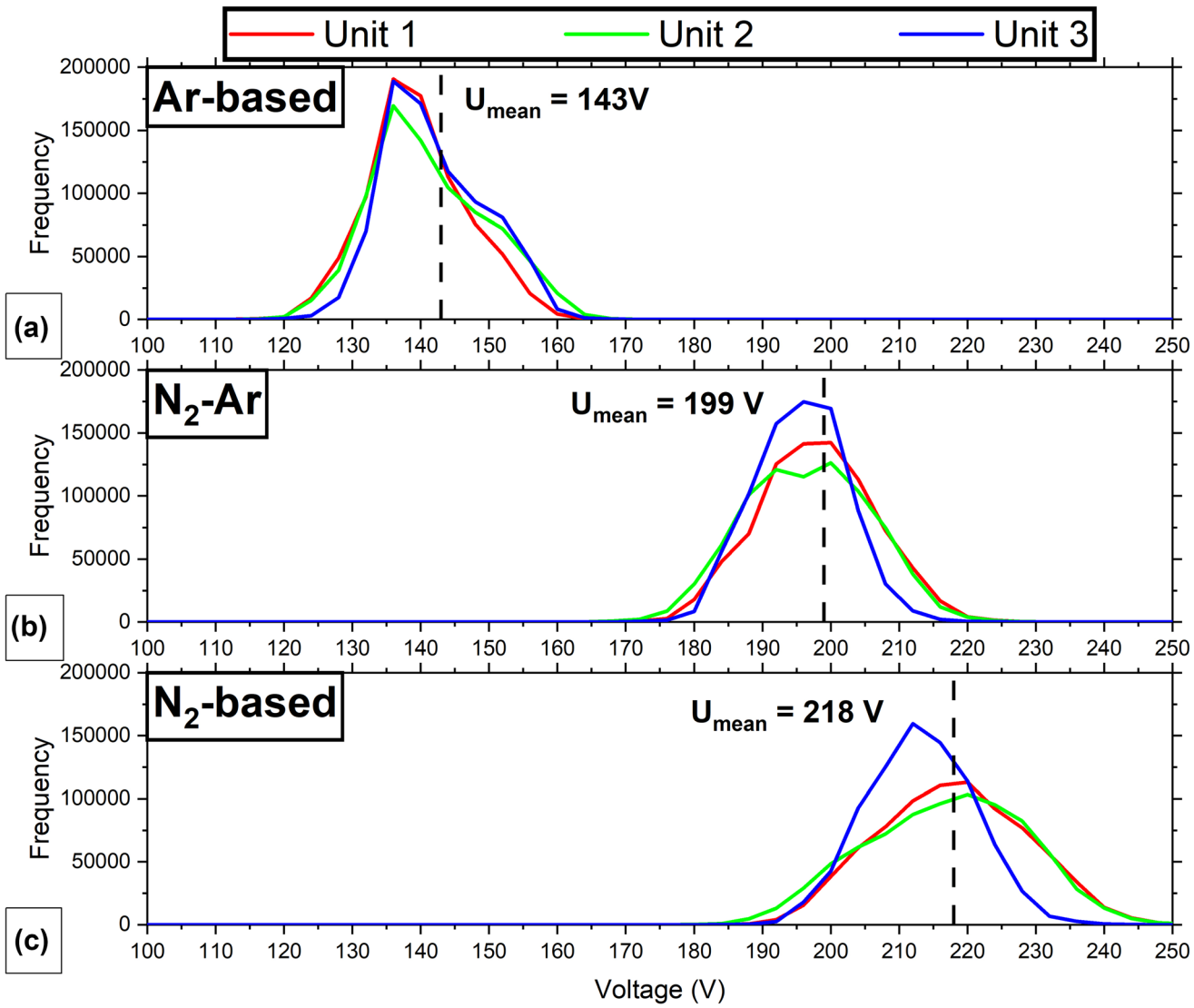

Fig. 3 Frequency distribution of the voltage for the Ar-based (a), N_2-Ar (b) and N_2-based (c) of the 5/16″ nozzle case without suspension

distributions also showed some asymmetry. Calculating the power for each individual measurement point yields a distribution of the total power with the sampling rate, as explained in the 'Experimental Methods' section. Here, the above-mentioned effects overlap. Overall, however, it can be said that the distribution of the power data is primarily determined by the respective voltage values, which is reflected in graphs similar to the voltage distribution. The voltage distribution can therefore be considered representative for this type of measurement.

The voltage over time of each plasma generator unit for the different gas composition is shown in Fig. 4(a). There are no major differences between the individual plasma generators. The average values scale with the thermal conductivity of the gas composition. However, fluctuations in the individual values are evident in the frequency distribution but not accurately represented in the mean values nor the standard deviation. To better characterize the internal deviation of the voltage frequency distribution, Fig. 4(b) shows the arithmetic deviation of the time course of the voltage, $R_{a,Volt}$ (following the standardized roughness nomenclature). The arithmetic deviation is more robust to individual events and therefore represents the whole variation better in comparison with the maximum deviation, $R_{z,Volt}$. From here on, the expression "voltage roughness" is used for $R_{a,Volt}$.

For each plasma generator unit, the voltage roughness has been evaluated over the three conditions. By evaluating $R_{a,Volt}$ it becomes apparent that the respective voltage deviation now better correlates with the findings from the frequency distribution. For both Unit 1 and 2, the voltage roughness scales in a consistent ratio with the increased power supply over the respective gas mixture to a larger extent. However, Unit 3 does not follow the trend and

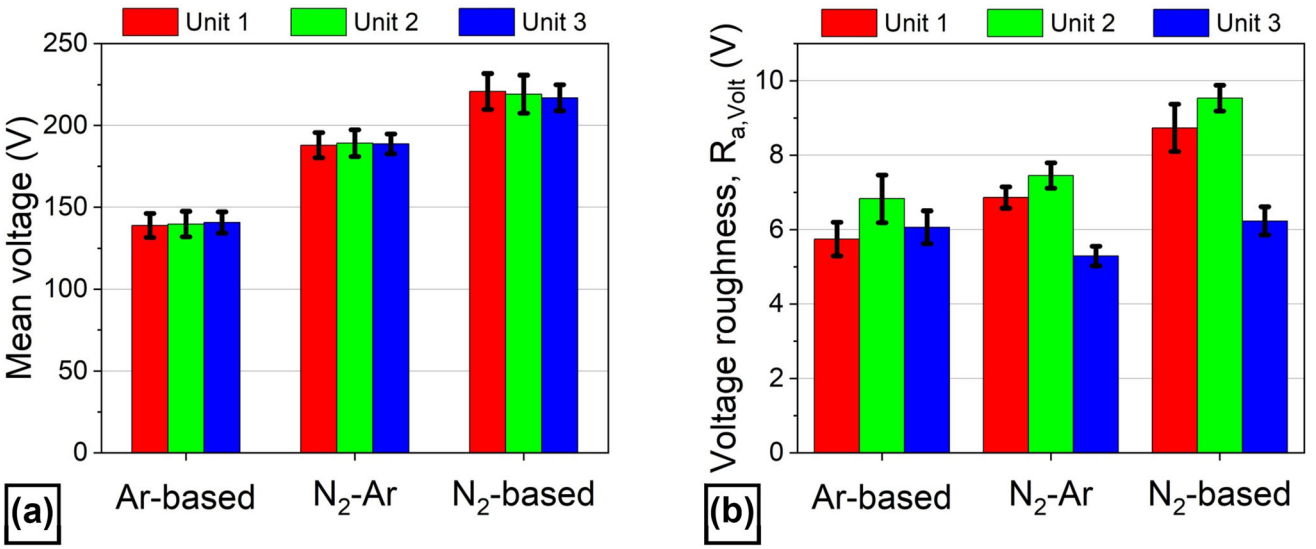

Fig. 4 Mean voltage (a) and voltage roughness (b) of the 5/16″ nozzle for all three plasma conditions

varies between the three gas compositions, exceeding the range of statistical variation. For the cases with highest thermal conductivity, the voltage roughness does not indicate a significant increase. It is important to emphasize that the roughness is obtained as the mean value from the raw data over each of the 10 stacks, including the corresponding standard deviation. As presented in the frequency distribution, one could assume that the large amount of spikes in the blue line indicate an increased roughness. However, this is a misleading assumption and can be explained by the decreased width of the Gaussian distribution. As an example, in the N_2-based case, the voltage values for Unit 3 have a decreased range (approx. 195-235 V) and vary less compared to Unit 1 and 2 (approx. 195-245 V). Similar findings can be obtained for the N_2-Ar case. The asymmetric behavior, visible in the voltage frequency, of Unit 3 is therefore also present in the voltage roughness.

As previously indicated, analogous variations were obtained for the current of 220 A per electrode. Focusing on the significant variation in voltage, this behavior can be related directly to the results obtained for the transport coefficients of the three cases. As explained in the previous section, the respective gas compositions determine the specific properties of the plasma and influence the required voltage of the plasma generator. As observed for the power supply, the arithmetic deviation scales with the thermal conductivity level. The most pronounced variation is seen for the N_2-based case with the highest thermal conductivity of the plasma. Due to the energy transfer from the power source to the plasma, the arc begins to change its shape and resistance, resulting in significant fluctuations (Ref 18). This is also seen over all three generators, where the specific variations increase the total deviation. The magnitude of the voltage fluctuation scales down with decreasing thermal conductivity of the plasma and therefore reduced power supply, as observed for the other two cases. It should be noted that Unit 3 is contrary to the outcome described before. This might be a hint to an unregularly running mode of the plasma generator, yielding diverging results in the voltage values. However, no defects such as wear could have optically been identified (Ref 18).

Particle Diagnostics

As outlined in the 'Experimental Methods' section, the particle temperature and velocity were quantified using the Accuraspray 4.0. Since the same parameters and nozzle were used in all coating experiments, except the gas composition, it is reasonable to conclude that the particle properties are correlated with the transport coefficients of the plasmas. Figure 5(a) shows the particle temperatures for all three cases. The modeling of the transport coefficients indicated a significantly reduced thermal conductivity for the Ar-based case. In line with these findings, the particles exhibit the lowest average temperature of about 2800 °C. As expected, the particles of the N_2-Ar case are considerably higher at about 3080 °C. The N_2-based case, which exhibits the highest thermal conductivity and plasma energy, gives an elevated particle temperature of about 3150 °C. In general, the ascending order of the particle temperature across the three parameters is consistent with the findings from the power and voltage data for each condition, as well as the results from the calculations of the thermal conductivity.

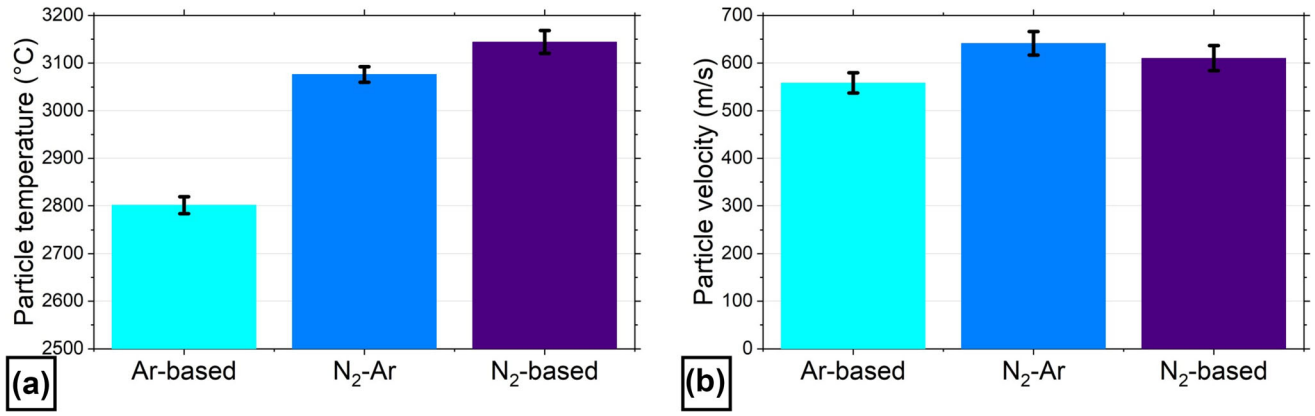

Fig. 5 Particle temperature (a) and velocity (b) of the 5/16″ nozzle, measured via Accuraspray 4.0, for all three cases

A similar distinction between the measured values is not evident for the particle velocity in Fig. 5(b). All three cases are close together, with a value of about 600 m/s. Furthermore, the error bars partially overlap. It is expected that the highest particle velocity would be observed for the N_2-based case with the highest power input, resulting in the highest acceleration of the particles through the plasma. However, no clear correlation of particle velocities with plasma power was observed. In particular, the particle diameters involved in SPS are typically very small. Therefore, low Reynolds particle numbers are assumed. Considering the drag force acting on a particle as dominant, allows us to describe the movement of the particles using the "drag law". Combined with the definition of the drag coefficient applicable to low particle Reynolds numbers (Stokes regime), the particle density is eliminated from the governing expression for the drag force (Ref 26). This indicates that the particle motion in such plasma regimes is primarily determined by the viscosity of the fluid, which does not vary significantly between the three cases.

Considering the available data, it is not appropriate to directly attribute the observed particle velocities to the plasma condition. Since the particle velocity did not fluctuate greatly across the different gas compositions, this could also be attributed to the same expansion ratio in each case. However, the particle temperature measurements already showed a high degree of correlation with the conclusions derived from the thermal conductivity and power data. Since the temperature of the impacting splats is a crucial factor for the deposition efficiency in SPS, the observed results should also be reflected in the corresponding coatings.

Coating Properties

For each condition, spray experiments were carried out using the three gas compositions. First, the 5/16″ nozzle has been used. Figure 6(a) depicts the cross section for the N_2-based case. The particle diagnostics indicated the highest particle temperatures, which were accompanied by a correspondingly high thermal conductivity and plasma energy. At these elevated temperatures, the particles are expected to melt to a greater extent than under other conditions. Furthermore, the high thermal conductivity extends the high-temperature isotherms, which results in an increased surface temperature $T_{S,n1,III}$ = 170 °C for the N_2-based case.

This results in good adhesion of the coating to the stainless steel substrate, as shown in the microstructure by the largely defect-free interface. The coating thickness $t_{c,n1,III}$ for this parameter is approximately 145 µm with a $DE_{n1,III}$ of approximately 64%. It is evident that the coating has significant vertical cracking. In thermal barrier coatings (TBC), these are referred to as dense vertical cracks (DVC) or segmentation cracks (Ref 27). This phenomenon is caused by the cooling of the hot splats on the typically cooler substrate or the previously deposited layer. As the splats cool down, they induce residual tensile stresses in the typically dense layers, whose porosity between the cracks is $Por_{a,n1,III} = 3.2 \pm 0.2\%$. During the deposition process, these induced stresses accumulate until vertical cracking occurs. Occasionally, a corresponding crack propagation in the horizontal direction can be observed, with the cracks following the interface of each layer. Partwise, the total number of 20 coating cycles can be observed.

The increased temperature of the splats is also reflected in the surface topography. Figure 6(b) depicts the surface topography for the N_2-based case. At the edges, the imprints of the sample holder are visible, as well as isolated coating detachments. As previously mentioned in the method section, a one-second pause was included between the coating meanders to facilitate the reduction of the temperature in the coating.

The observed coating detachment indicates that the temperature is too high, resulting in the presence of

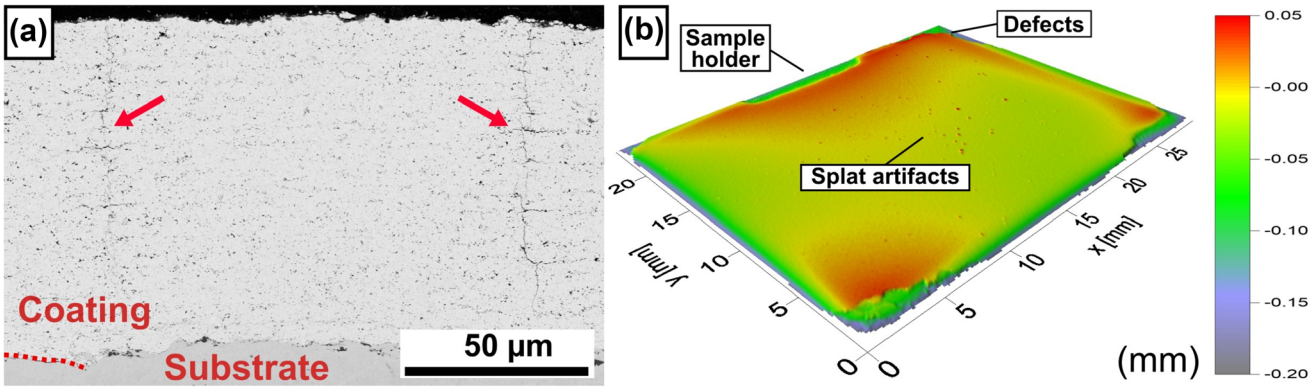

Fig. 6 SEM-BSE image of the coating microstructure (a) and topography (b) of the 5/16″ nozzle, obtained with the N_2-based case. The segmentation cracks are indicated by red arrows. (Color figure online)

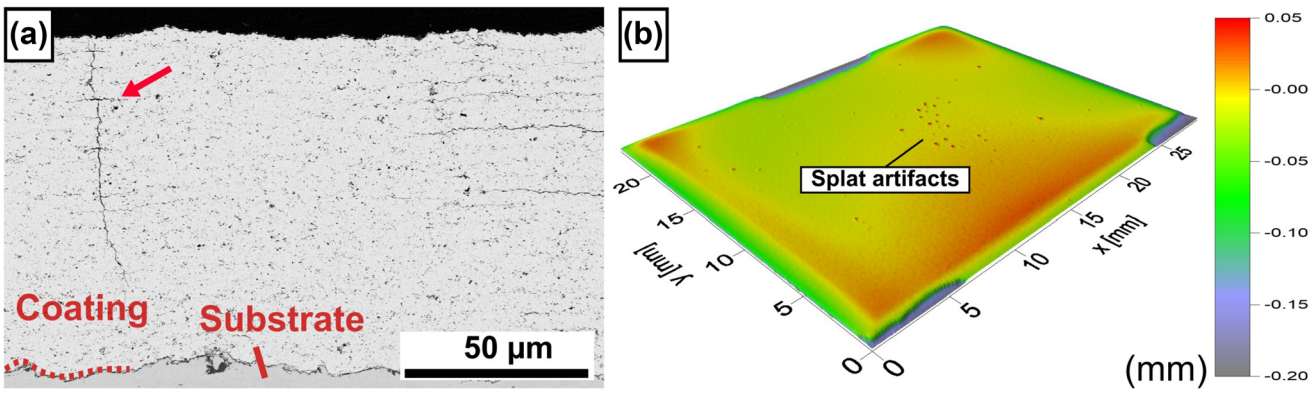

Fig. 7 SEM-BSE image of the coating microstructure (a) and topography (b) of the 5/16″ nozzle, obtained with the N_2-Ar case. The segmentation cracks are indicated by red arrows. (Color figure online)

residual tensile stresses in the coating. The roughness of the coating is $R_{a,n1,III} = 1.9 \pm 0.6$ µm. In addition, only isolated splat artifacts are visible on the surface, which may represent splashes caused by the impact of cooled splats. It is reasonable to assume that the observed splat artifacts may be a possible reason for the large standard deviation of the measured surface roughness.

The N_2-Ar case in Fig. 7(a) shows a comparable microstructure, which is consistent with the findings of the modeling and diagnostic results. The segmentation cracks are also visible in this case. A coating thickness of $t_{c,n1,II} = 136$ µm is in accordance with the reduced particle temperature of the splats, as determined by Accuraspray measurements and calculation of the transport coefficients. The slightly increased $DE_{n1,II}$ of approximately 66% compared to the N_2-based case was related to the isolated coating detachment, as already shown before. No significant difference in size or frequency of the segmentation cracks could statistically be proven for both cases although they are still visible; however, the porosity between the vertical cracks increased slightly to $Por_{n1,II} = 4.2 \pm 0.1\%$. In addition, the interface is more pronounced compared to the N_2-based case at a decreased surface temperature of $T_{S,n1,II} = 140$ °C. Consequently, the observed results are in good agreement with the decreased thermal conductivity of the plasma and the lower particle temperature compared to the N_2-based case.

The surface of the N_2-Ar case in Fig. 7(b) shows a topography that is analogous to that observed for the N_2-based case. Impressions of the clamps can also be observed in this case. However, there is no significant delamination occurring at the edge, indicating a generally lower process temperature related to isolated coating detachments as observed for the N_2-based case. Additionally, isolated artifacts, resulting from the incoming splats, can be seen on the surface. The roughness in this case is $R_{a,n1,II} = 1.9 \pm 0.6$ µm. Again, the large standard deviation of the surface roughness is assumed to be influenced by the observed splat artifacts. Overall, the investigation of microstructure and topography corroborates the diagnostic results.

The most notable differences in the calculation and diagnostic results were observed for the Ar-based case, which showed significantly reduced thermal conductivity, plasma energy, and particle temperature. Hence, the lowest particle temperature and the surface temperature were observed ($T_{S,n1,I}$ = 80 °C). The microstructure did not yield any vertical cracks, and the transition between the individual layers is barely recognizable (see Fig. 8a). It is evident that the temperature difference between the impacting splats and the substrate is insufficient to induce the required residual tensile stresses during the cooling process. Furthermore, he lower particle temperature is also indicated by an increased porosity of $Por_{n1,I}$ = 5.5 ± 0.3%. In contrast, the interface is clearly distinguishable based on its pronounced, black area. Due to the lower plasma and surface temperature, it is assumed that the splats do not melt to the same extent as with the other parameters. Consequently, the contact area on the roughened substrate will be smaller. This results in an overall reduction in coating adhesion. In this context, the coating thickness $t_{c,n1,I}$ decreased to approximately 90 µm, resulting in a $DE_{n1,I}$ of approximately 49%. As demonstrated by Singh et al. (Ref 28), the residual stress increase with a decrease in coating thickness. The Ar-based case had the lowest coating thickness out of the three cases. This finding suggests that the temperature difference, and thus residual stress, resulting from the increased Argon content was not sufficient to cause vertical cracks.

Similarly, the effect of the reduced processing temperatures, as seen in the microstructure, is also evident in the topography of the coating. With regards to the Ar-based case, the most uniform surface can be observed due to the splats that may impact in a rather viscous state (see Fig. 8b). This is indicated by the lowest roughness of $R_{a,n1,I} \approx 1.1$ µm. Furthermore, isolated splatters, which occurred at the higher temperatures, are not visible, resulting in a low standard deviation.

7/16″ Nozzle

Current and Voltage Measurements

In the framework of the present study, an additional measurement of current and voltage has been carried out for the 7/16″ nozzle using the N_2-Ar case. All other settings stay the same.

As shown in Fig. 9(a), the mean voltage does not vary significantly between the individual units and has marginally decreased compared to the 5/16″ nozzle with respect to the overlapping error bars ($\Delta V_{m,n1\text{-}n2,II} \approx 10$ V). Similar findings can be obtained for the voltage roughness in Fig. 9(b). In comparison with the results previously obtained for the 5/16″ nozzle, the 7/16″ nozzle exhibited slightly decreased roughness values and thus fluctuation of the voltage data ($\Delta R_{a,Volt,n1\text{-}n2,II} \approx$ 0.8-0.4 V).

Using the same current (220 A), the ratio between the three plasma generator units remains consistent in both results. However, even if the error bars partially overlap, a descendant trend of the overall voltage for the 7/16″ nozzle can be observed. As stated in the 'Experimental methods' section, the expansion ratio of the 7/16″ nozzle is decreased, which is assumed to reduce the overall gas and plasma velocity. Consequently, the gas is expected to move away from the plasma generators more slowly and increase the residence time of the particles. This in turn leads to an increased gas density at the plasma generators. In addition, the increased drag force is expected to elongate the electric arc. These combined effects are thus estimated to result in a lower required voltage to achieve the desired current. The voltage data, using the N_2-Ar-based case is summarized in Table 3.

Particle Diagnostics

The previously mentioned decreased expansion ratio of the 7/16″ nozzle is also expected to affect the particle

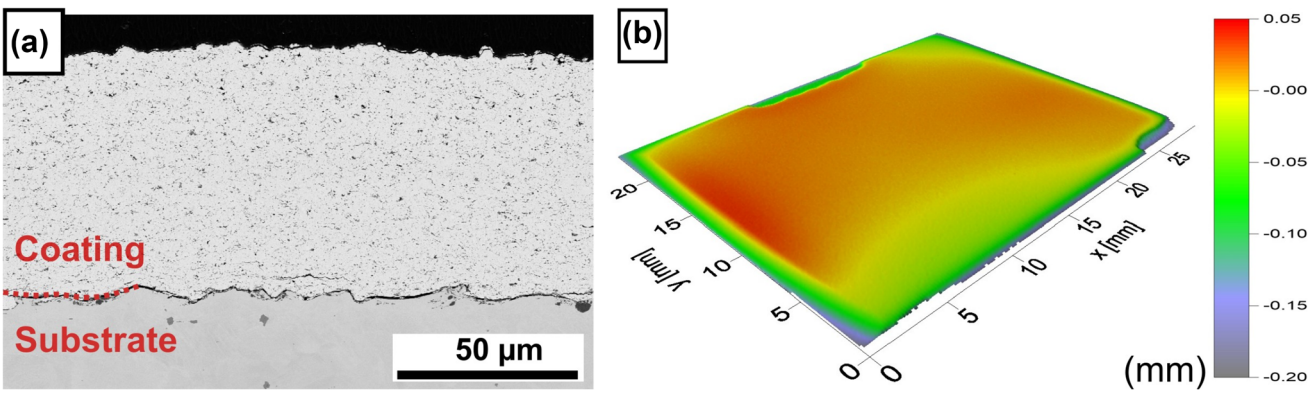

Fig. 8 SEM-BSE image of the coating microstructure (a) and topography (b) of the 5/16″ nozzle, obtained with the Ar-based case

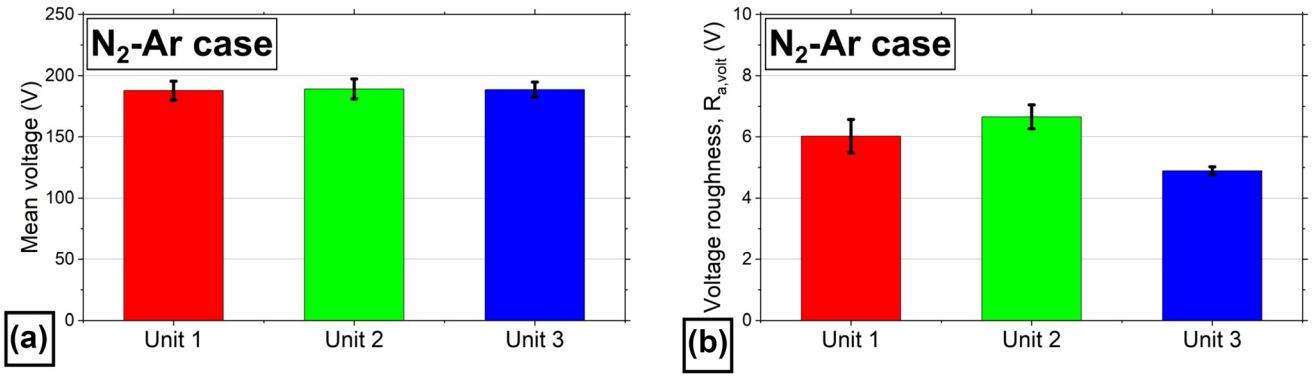

Fig. 9 Voltage mean values (a) and roughness $R_{a,Volt}$ (b) of the 7/16″ nozzle for the N_2-Ar case, respectively

Table 3 Mean voltage and roughness per generator unit for the two nozzles using the N_2-Ar-based case

Generator	Nozzle	Mean voltage, V_m, V	Voltage roughness, $R_{a,Volt}$, V
Unit 1	5/16″	201.41 ± 8.22	6.86 ± 0.28
	7/16″	187.92 ± 7.72	6.02 ± 0.55
Unit 2	5/16″	200.40 ± 9.25	7.45 ± 0.34
	7/16″	189.18 ± 8.20	6.65 ± 0.39
Unit 3	5/16″	199.21 ± 6.55	5.29 ± 0.27
	7/16″	188.70 ± 6.10	4.89 ± 0.13

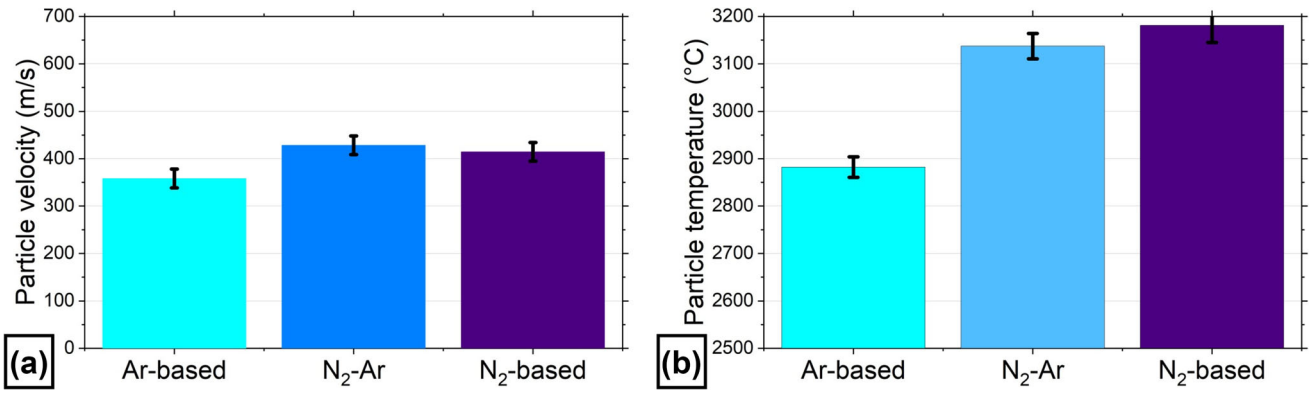

Fig. 10 Particle temperature (a) and velocity (b) of the 7/16″ nozzle, respectively, for all three cases

properties. The same measurements using the Accuraspray 4.0 have been carried out for both nozzles and all three cases.

The effect of the varied nozzle geometry is less significant for the particle temperature, as shown in Fig. 10(a). The reduced expansion ratio is expected to increase plasma temperatures which will increase the particle temperatures ($\Delta T_{p,n1\text{-}n2} \approx$ 40-80 °C). This difference is less pronounced compared to the particle velocity but it is still apparent. The ratio of the thermal expansion coefficients across the three cases is also present for both nozzles.

Figure 10(b) illustrates the particle velocity of the three cases using the 7/16″ nozzle. The explanations provided in the previous chapter can also be applied to the realm of particle diagnostics. According to the reduced plasma velocity due to the lower expansion ratio, the particle velocity results in a substantial decline for the 7/16” nozzle ($\Delta v_{p,n1\text{-}n2} \approx$ 200 m/s). Moreover, the ratio between each case remains constant. Consequently, it can be assumed that the effect of the respective transport coefficient remains evident, particularly with regard to the thermal conductivity. All particle data are summarized in Table 4.

Coating Properties

The previously obtained results for the 7/16″ nozzle are expected to affect the coating properties in comparison with the 5/16″ nozzle. Again, the same procedure in terms

Table 4 Particle temperature and velocity for each case and both nozzles

Case	Nozzle	Particle velocity, v_p, m/s	Particle temperature, T_p, °C
I	5/16″	558.45 ± 21.06	2801.56 ± 17.56
Ar-based	7/16″	358.21 ± 19.92	2882.24 ± 21.69
II	5/16″	641.42 ± 25.07	3076.52 ± 16.34
N_2-Ar	7/16″	428.50 ± 19.57	3137.23 ± 26.65
III	5/16″	610.21 ± 26.42	3144.38 ± 24.15
N_2-based	7/16″	414.71 ± 19.67	3181.29 ± 36.40

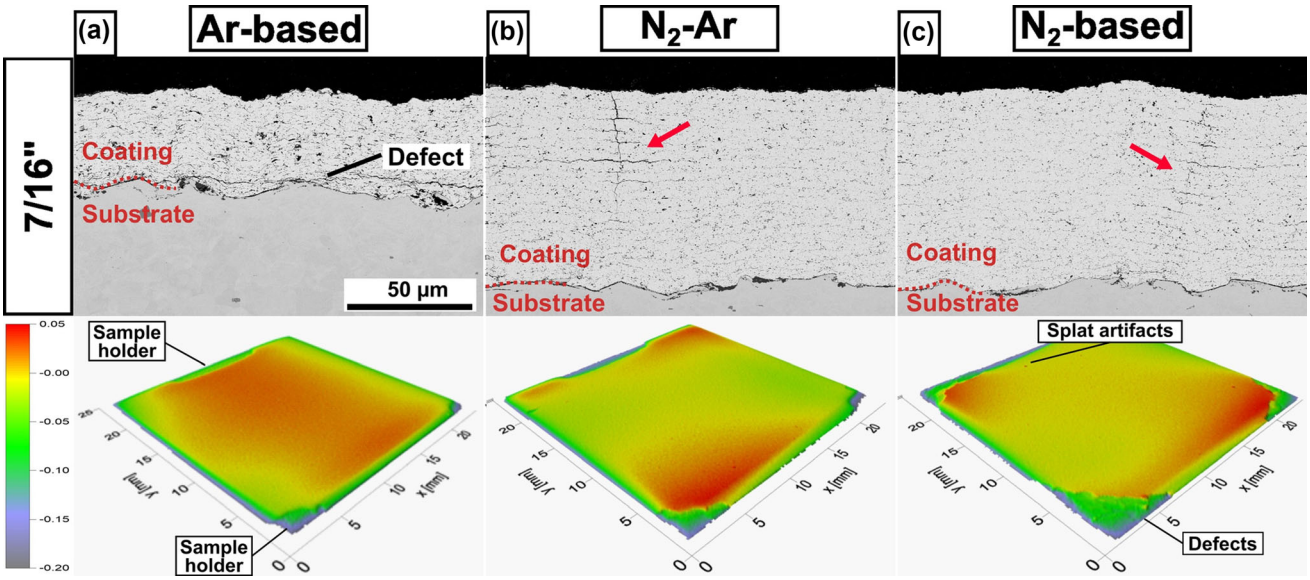

Fig. 11 Microstructure and topography for the three cases (a, b, c) in horizontal direction, respectively, using the 7/16″ nozzle. The segmentation cracks are indicated by red arrows. (Color figure online)

of microstructural and topographical analyses have been conducted for each coating. As the single results per case have already been shown for the 5/16″ nozzle, Fig. 11 presents an overview of microstructure and topography for the three cases using the 7/16″ nozzle. The scalebars have been kept constant.

The particle diagnostics already showed an increased particle and, therefore, process temperature. The result is in line with the surface temperature measured using a pyrometer. This showed that both the N_2-Ar and N_2-based cases increased the process temperature by 30 and 50 °C, respectively. However, neither the spray distance nor the surface scanning speed have been changed. As mentioned earlier, higher process temperatures can lead to increased residual tensile stresses in the coating. In addition, the splats impact at a lower velocity due to the decreased plasma velocity. Based on the results, the reduced impact velocity of the splats is more significant than the increased temperature. These combined effects are reflected in a decreased deformability of the incoming splats and thus a reduced adhesion quality. This is particularly evident at the interface of each coating, which is more pronounced for the 7/16″ nozzle compared to the 5/16″ nozzle ones. The coating properties from both nozzles for the three cases are summarized in Table 5.

The resulting coating thickness is thus significantly decreased for the Ar-based case, where cold splats impact at high velocity ($t_{c,n2,I}$ = 47 µm, $DE_{n2,I}$ = 24%). The low adhesion quality even results in defects, as shown in Fig. 11(a). The porosity has significantly increased compared to the 5/16″ nozzle ($Por_{n2,I}$ = 9.1 ± 0.8%). The microstructure further indicates an uneven surface yielding an increased roughness for the low deformable spats ($R_{a,n2,I}$ = 2.9 ± 0.1 µm). It should be noted that the overall temperature of the Ar-based case is again not sufficient to induce segmentation cracks in the coating.

Also, for the N_2-Ar case in Fig. 11(b), the process efficiency has significantly decreased due to the effects outlined before, but still higher than the Ar-based case ($t_{c,n2,II}$ = 118 µm, $DE_{n2,II}$ = 52%). Due to the increased plasma temperature, the better deformable splats yield an increased bonding quality. This is evident in the lower

Table 5 Deposition efficiency (DE), coating thickness (t_c), roughness (R_a), porosity (Por) and surface temperature (T_S) for each case and both nozzles

Case	Nozzle	DE, %	t_c, µm	R_a, µm	Por, %	T_S, °C
I	5/16″	49	90	1.1 ± 0.0	5.5 ± 0.3	80
Ar-based	7/16″	24	47	2.9 ± 0.1	9.1 ± 0.8	80
II	5/16″	66	136	1.9 ± 0.6	4.2 ± 0.1	140
N_2-Ar	7/16″	52	118	2.6 ± 0.2	4.7 ± 0.3	170
III	5/16″	64	145	1.9 ± 0.6	3.2 ± 0.2	170
N_2-based	7/16″	52	146	2.3 ± 0.1	4.0 ± 0.3	220

porosity ($Por_{n2,II}$ = 4.7 ± 0.3%), which is still above the value for the 5/16″ nozzle. The increased plasma temperature consequently results in the presence of segmentation cracks in the coating. The same principle applies to the surface roughness ($R_{a,n2,II}$ = 2.6 ± 0.2 µm). Another outcome is the non-presence of isolated splat artifacts, which have been obtained for the 5/16″ nozzle. It is thus estimated that the absence of segmentation cracks is also related of the decreased splat velocity upon impact preventing such splashes. That estimation is further supported by the reduced standard deviation of the measured surface roughness.

According to the trend from the thermal conductivity, the N_2-based parameter results in the largest coating thickness at simultaneously reduced DE due to the edge delamination, as observed for the 5/16″ nozzle ($t_{c,n2,III}$ = 146 µm, $DE_{n2,III}$ = 52%). The decrease in the DE scales with the increase in the process temperature, which was the largest for the N_2-based case and still causes segmentation cracks from the induced residual tensile stresses. The hot incoming splats are assumed to yield the best deformability, which results in the lowest porosity for the three cases but still higher compared to the 5/16″ nozzle due to the lower impact velocity ($Por_{n2,III}$ = 4.0 ± 0.3%). However, contrary to the N_2-Ar case, the splat temperature is obviously high enough to compensate for the low impact velocity and thus produce a very low amount of isolated splat artifacts ($R_{a,n2,III}$ = 2.3 ± 0.1 µm).

The coating properties demonstrate a strong correlation with the findings from the process diagnostics. Furthermore, the ratio of the three gas compositions for both nozzles was found to be in close agreement, yielding the same ratio. It is evident that the data obtained from the measurement of voltage, as well as from diagnostic analyses and coating analyses, are generally consistent with the initially calculated transport coefficients. This is particularly apparent in the case of thermal conductivity. Consequently, additional experiments on different nozzle geometries or a shifted plasma generator setup, such as individual power supply, can empirically be compared to the established setup. It is therefore concluded that the implementation of such a procedure will facilitate a more profound comprehension of the Axial III^{TM} torch, thereby enhancing process stability and efficiency in the future.

Conclusion

As part of this study, the Axial III^{TM} torch was analyzed for a range of gas compositions with respect to their plasma properties using two different nozzle geometries. Diagnostics were performed using the current/voltage data available from the plasma generators and in-flight particle diagnostics. Furthermore, cross sections and topography of the coatings were examined, as sprayed under different plasma compositions. The results can be summarized as follows:

- The three intensity lobes are apparent for the three gas compositions, as shown by the voltage measurements of the individual plasma generators. Each generator caused individual fluctuations, which were attributed to the formation of the electric arc.
- The thermal conductivity of the plasma was identified as a crucial parameter for the spray process. It was found that the thermal conductivity increases with the molecular fraction of the gas composition, in particular with the hydrogen content.
- Thermal conductivity was linked to voltage measurements and particle properties observed by in-flight diagnostics. The highest conductivity caused the largest voltage fluctuations and the highest particle temperature.
- For each nozzle diameter, the gas composition with the highest thermal conductivity produced the lowest porosity, the best adhesion, and the highest coating thickness. Segmentation cracks can be prevented by adding argon, which has a lower thermal conductivity but results in lower DE and less dense coatings.
- The experiments with the 7/16″ nozzle showed that a lower expansion ratio reduces process efficiency, primarily because of the lower impact velocity of the splats. The voltage, particle diagnostics, and coating properties for the three gas compositions showed consistent scaling with the nozzle.

Acknowledgment This work was funded by the Deutsche Forschungsgemeinschaft (DFG, German Research Foundation)—project number 501838742. The authors would like to thank Mr. Karl-Heinz Rauwald for operating the spray facility and Dr. Doris Sebold for the scanning electron microscopy imaging.

Funding Open Access funding enabled and organized by Projekt DEAL.

References

1. D.A. Ross and A. Burgess, Plasma Jet Converging System, 1996.
2. Axial III Core Technology | Northwest Mettech Corp. 2025, https://www.mettech.com/coating-technology/axial-III-core-technology.php. Accessed 10 Jan 2025.
3. P. Fauchais, Understanding Plasma Spraying, *J. Phys. D Appl. Phys.*, 2004, **37**(9), p R86–R108.
4. J. Schein, J. Zierhut, M. Dzulko, G. Forster and K.D. Landes, Improved Plasma Spray Torch Stability Through Multi-Electrode Design, *Contrib. Plasma Phys.*, 2007, **47**(7), p 498–504.
5. C. Moreau, P. Gougeon, A. Burgess, and D. Ross, Characterization of Particle Flows in an Axial Injection Plasma Torch, ASM Int., 1995.
6. J. Mostaghimi and M.I. Boulos, Thermal Plasma Sources: How Well Are They Adopted to Process Needs?, *Plasma Chem. Plasma Process.*, 2015, **35**(3), p 421–436.
7. P. Fauchais, M. Vardelle, S. Goutier and A. Vardelle, Key Challenges and Opportunities in Suspension and Solution Plasma Spraying, *Plasma Chem. Plasma Process.*, 2015, **35**(3), p 511–525.
8. A. Ganvir, R.F. Calinas, N. Markocsan, N. Curry and S. Joshi, Experimental Visualization of Microstructure Evolution During Suspension Plasma Spraying of Thermal Barrier Coatings, *J. Eur. Ceram. Soc.*, 2019, **39**(2–3), p 470–481.
9. B.R. Marple, R.S. Lima, C. Moreau, S.E. Kruger, L. Xie and M.R. Dorfman, Yttria-Stabilized Zirconia Thermal Barriers Sprayed Using N2–H2 and Ar-H2 Plasmas: Influence of Processing and Heat Treatment on Coating Properties, *J. Therm. Spray Technol.*, 2007, **16**(5–6), p 791–797.
10. R.S. Lima, B.M.H. Guerreiro, N. Curry, M. Leitner and K. Körner, Environmental, Economical, and Performance Impacts of Ar-H2 and N2–H2 Plasma-Sprayed YSZ TBCs, *J. Therm. Spray Technol.*, 2020, **29**(1–2), p 74–89.
11. C. Ruelle, S. Goutier, V. Rat, A. Keromnes, C. Chazelas and É. Meillot, Study of the Electric Arc Dynamics in a Cascaded-Anode Plasma Torch, *Surf. Coat. Technol.*, 2023, **462**, 129493.
12. M. Gaudin, S. Goutier, G. Rivaud, A. Joulia, E. Béchade and A. Kéromnès, Diagnostic of the Liquid Injection Behavior in the Case of Axial Suspension Plasma Spray (ASPS), *J. Therm. Spray Technol.*, 2024, **34**, p 753–764.
13. J.K. Perambadur, V. Rat, T.N. Niane and C. Chazelas, Simulation of the Axial III Plus Plasma Torch and Its Arc Fluctuations, *J. Therm. Spray Technol.*, 2024, **33**, p 2526–2547.
14. J. Lee, S.-J. Park, Y.-S. Oh, S. Kim, H. Kim and S.-M. Lee, Fragmentation Behavior of Y_2O_3 Suspension in Axially Fed Suspension Plasma Spray, *Surf. Coat. Technol.*, 2017, **309**, p 456–461.
15. F. Tarasi, M. Medraj, A. Dolatabadi, J. Oberste-Berghaus and C. Moreau, Effective Parameters in Axial Injection Suspension Plasma Spray Process of Alumina-Zirconia Ceramics, *J. Therm. Spray Technol.*, 2008, **17**(5–6), p 685–691.
16. F. Tarasi, M. Medraj, A. Dolatabadi, J. Oberste-Berghaus and C. Moreau, Phase Formation and Transformation in Alumina/YSZ Nanocomposite Coating Deposited by Suspension Plasma Spray Process, *J. Therm. Spray Technol.*, 2010, **19**(4), p 787–795.
17. S. Zimmermann, G. Mauer, K.-H. Rauwald and J. Schein, Characterization of an Axial-Injection Plasma Spray Torch, *J. Therm. Spray Technol.*, 2021, **30**(7), p 1724–1736.
18. G. Mauer, Multiple Electrodes and Cascaded Nozzles: A Review of the Evolution of Modern Plasma Spray Torches, *J. Therm. Spray Technol.*, 2024, **34**, p 484–494.
19. A. Farrokhpanah, T.W. Coyle and J. Mostaghimi, Numerical Study of Suspension Plasma Spraying, *J. Therm. Spray Technol.*, 2017, **26**(1–2), p 12–36.
20. H.-B. Jung, J.-I. Park, S.-H. Park, H.-J. Kim, C. Lee and J.-W. Han, Effect of the Expansion Ratio and Length Ratio on a Gas-Particle Flow in a Converging-Diverging Cold Spray Nozzle, *Met. Mater. Int.*, 2009, **15**(6), p 967–970.
21. J. Schindelin, I. Arganda-Carreras, E. Frise, V. Kaynig, M. Longair, T. Pietzsch, S. Preibisch, C. Rueden, S. Saalfeld, B. Schmid, J.-Y. Tinevez, D.J. White, V. Hartenstein, K. Eliceiri, P. Tomancak and A. Cardona, Fiji: An Open-Source Platform for Biological-Image Analysis, *Nat. Methods*, 2012, **9**(7), p 676–682.
22. A. Akbarnozari, F. Ben-Ettouil, S. Amiri, O. Bamber, J.-D. Grenon, M. Choquet, L. Pouliot and C. Moreau, Online Diagnostic System to Monitor Temperature of In-Flight Particles in Suspension Plasma Spray, *J. Therm. Spray Technol.*, 2020, **29**(5), p 908–920.
23. S. Gordon and B.J. McBride, Computer Program for Calculation of Complex Chemical Equilibrium Compositions and Applications, 1994.
24. M.I. Boulos, P.L. Fauchais and E. Pfender, *Handbook of Thermal Plasmas*, Springer, Cham, 2023.
25. G. Mauer, J.-L. Marqués-López, R. Vaßen and D. Stöver, Detection of Wear in One-Cathode Plasma Torch Electrodes and Its Impact on Velocity and Temperature of Injected Particles, *J. Therm. Spray Technol.*, 2007, **16**(5–6), p 933–939.
26. A. Nastic and B. Jodoin, Evaluation of Heat Transfer Transport Coefficient for Cold Spray Through Computational Fluid Dynamics and Particle In-Flight Temperature Measurement Using a High-Speed IR Camera, *J. Therm. Spray Tech.*, 2018, **27**(8), p 1491–1517.
27. E. Bakan and R. Vaßen, Ceramic Top Coats of Plasma-Sprayed Thermal Barrier Coatings: Materials, Processes, and Properties, *J. Therm. Spray Technol.*, 2017, **26**(6), p 992–1010.
28. R. Singh, S. Schruefer, S. Wilson, J. Gibmeier and R. Vassen, Influence of Coating Thickness on Residual Stress and Adhesion-Strength of Cold-Sprayed Inconel 718 Coatings, *Surf. Coat. Technol.*, 2018, **350**, p 64–73.